JASA **ARTICLE**

Probabilistic inversion for submerged source depth and strength from infrasound observations

Gil Averbuch,[1,a),b)] Roger M. Waxler,[2] Pieter S. M. Smets,[1,c)] and Läslo G. Evers[3,d)]

[1]*Department of Geoscience and Engineering, Faculty of Civil Engineering and Geosciences, Delft University of Technology, 1 Stevinweg Street, Delft, The Netherlands*

[2]*NCPA, University of Mississippi, Oxford, Mississippi, USA*

[3]*R&D Department of Seismology and Acoustics, Royal Netherlands Meteorological Institute, 201 Postbus Street, De Bilt, The Netherlands*

ABSTRACT:

In seismology, the depth of a near-surface source is hard to estimate in the absence of local stations. The depth-yield trade-off leads to significant uncertainties in the source's depth and strength estimations. Long-range infrasound propagation from an underwater or underground source is very sensitive to variations in the source's depth and strength. This characteristic is employed in an infrasound based inversion for the submerged source parameters. First, a Bayesian inversion scheme is tested under the variations of the number of stations, the signal's frequency band, and the signal-to-noise ratio (SNR). Second, an ensemble of realistic perturbed atmospheric profiles is used to investigate the effect of atmospheric uncertainties on the inversion results. Results show that long-range infrasound signals can be used to estimate the depth and strength of an underwater source. Using a broadband signal proved to be a fundamental element to obtain the real source parameters, whereas the SNR was secondary. Multiple station inversions perform better than one-station inversions; however, variations in their position can lead to source strength estimations with uncertainties up to 50%. Regardless of the number of stations, their positions, and SNRs, all of the estimated depths were within 10% from the real source depth. © 2020 Acoustical Society of America. https://doi.org/10.1121/10.0000695

I. INTRODUCTION

Since the 1940s, efforts have been made to study the acoustic and seismic response of explosions.[1–4] Experimental, analytical, and numerical tests showed the effect of the explosion medium,[5] yield,[3] and depth[6,7] on the recorded seismic waves. Moreover, analytic and empirical methods have been developed to differentiate underground explosions from natural seismic activity as well as to estimate the explosion's source parameters (i.e., yield and depth). These methods are based on separating the different phases and estimating their time differences and relative amplitude ratios.[8–13] A depth-yield trade-off curve[14] usually links the explosion's source parameters. Consequently, an accurate estimation of one parameter provides the other.

The ability to separate the phases depends on the source depth and the recorded signal. For example, to distinguish between the direct P arrival and its free-surface reflection, Pp/s, their periods must be shorter than twice the travel time between the source and the Earth's surface. Therefore, for shallow sources, a common requirement is the presence of local or regional seismic stations. At these distances, the

required high-frequency components (that correspond to short periods) are preserved, allowing the capability to distinguish between the phases and making the source parameter estimation possible. In contrast, the low-frequency content that is recorded at teleseismic distances averts a proper separation of the phases, thus preventing an accurate estimation of the source parameters. The non-unique solution (depth-yield trade-off curve) and the uncertainties of the parameters lead to a broad spectrum of source parameter values.

Underground and underwater sources can also radiate low-frequency acoustic waves into the atmosphere. These waves are known as infrasound, and they can be trapped in the atmospheric waveguides and propagate over vast distances. Long-range infrasound signals from subsurface sources are usually attributed to earthquakes in an Earth-atmosphere[15–17] and Earth-ocean-atmosphere system,[18] as well as to underground nuclear explosions.[19] Seismic waves can be coupled into the atmosphere at the source epicenter (epicentral infrasound), at different regions along the seismic propagation path (secondary infrasound), and locally at the infrasound array due to ground-coupled air-waves.[20,21] Besides underwater and underground sources, infrasonic signals can be generated by natural and anthropogenic events; for example, explosions, ocean waves, and volcanic eruptions.[22]

The coupling of acoustic and seismic waves to infrasonic waves is associated with three types of waves that can be distinguished by their trace velocity (horizontal phase velocity). In an Earth-atmosphere and an ocean-atmosphere system, the first type of wave is a homogeneous P and S wave (body

---

a)Electronic mail: g.averbuch@tudelft.nl, ORCID: 0000-0002-0403-9354.

b)Also at: R&D Department of Seismology and Acoustics, Royal Netherlands Meteorological Institute, De Bilt, The Netherlands.

c)Also at: R&D Department of Seismology and Acoustics, Royal Netherlands Meteorological Institute, De Bilt, The Netherlands, ORCID: 0000-0003-0394-0973.

d)Also at: Department of Geoscience and Engineering, Faculty of Civil Engineering and Geosciences, Delft University of Technology, Delft, The Netherlands.

wave). Due to their relatively high trace velocities, the radiated waves propagate almost vertically upward, and cannot get trapped in the atmospheric waveguides. Therefore, their contribution to long-range infrasound propagation is minimal. The second type is an inhomogeneous P and S wave. Their low trace velocity leads to a large horizontal wavenumber component and an imaginary vertical wavenumber component. As a result, these waves experience an exponential decay in amplitude between the source and the ocean/Earth interface with the atmosphere. However, once in the atmosphere, they can propagate horizontally, get trapped in the atmospheric waveguides, and travel over hundreds or thousands of kilometers. Theory predicts that for a source in a distance of less than one acoustical wavelength from the interface with the atmosphere, the interface becomes transparent to the evanescent energy, meaning that all the evanescent energy can radiate into the atmosphere.[23–25] Moreover, it was shown that variation in the source depth leads to different radiation patterns in the atmosphere as well as changes in the total coupled energy.[23,24]

The third type of wave is a surface wave, and it exist in an Earth-atmosphere system. Depending on the Earth's and atmosphere's elastic and acoustic properties, surface waves can be recognized as leaky Rayleigh or Stoneley waves.[26,27] The surface wave velocity determines the direction of propagation in the atmosphere. For high surface wave velocity, the radiated wave will have a small horizontal wavenumber component; hence, it will propagate vertically upward. As the surface wave velocity decreases, the horizontal wavenumber component of the radiated wave increases, allowing the coupled wave to propagate horizontally and get trapped in the atmospheric waveguides. Analytical studies show that for a horizontally layered medium, inhomogeneous body waves and surface waves are the main contributors to the acoustic perturbations in the atmosphere with amplitudes up to three orders larger than from homogeneous body waves.[23–25]

The sensitivity of the coupled wave's amplitude to the source parameters leads us to the hypothesis that long-range infrasound signals can be used to invert for the underwater or underground source parameters. Assink *et al.* (2016)[19] made the first step and used infrasonic signals from North Korea's 2013 and 2016 underground nuclear tests to evaluate the relative source depth. Here, the prospect of an infrasound-based inversion, which extracts the submerged source's absolute depth and strength, is tested numerically. Inversion schemes in geophysics are a common practice for estimating an unknown set of parameters from observations.[28] They can be found in seismic tomography,[29] seismic wavefield reconstruction,[30] explosion yield estimation,[13,31] and evaluation of atmospheric properties.[32,33] Although it is used in different fields, the philosophy is similar: assuming a set of observations M, model parameters m, and a forward model G, one should find the model parameters that minimize the function $\|M - G(m)\|$.

The remainder of the paper concentrates on answering the following question: given an observed signal M, what are the submerged source's depth (z_s) and strength (S)? Our hypothesis is based on the sensitivity of the coupled evanescent body waves to variations in the source characteristics. This behavior belongs to both seismic and acoustic evanescent body waves.[23,25] Therefore, although this study focuses on submerged sources, the presented results can be useful also to subsurface sources. Section II describes the probabilistic inversion scheme as well as the Fast Field Program (FFP), which is the numerical model used to generate both "observed" signals and the dataset for the inversion scheme. Assuming a known atmospheric profile, Sec. III A shows the effect of the signal's frequency band, number of stations, and the signal-to-noise ratio (SNR) on the inversion results. Then, in Sec. III B, the effect of atmospheric uncertainties is investigated. The paper is concluded with a summary and a discussion of the results.

II. METHOD

Before diving into the inversion scheme, the possibility of overcoming the depth-yield trade-off needs to be
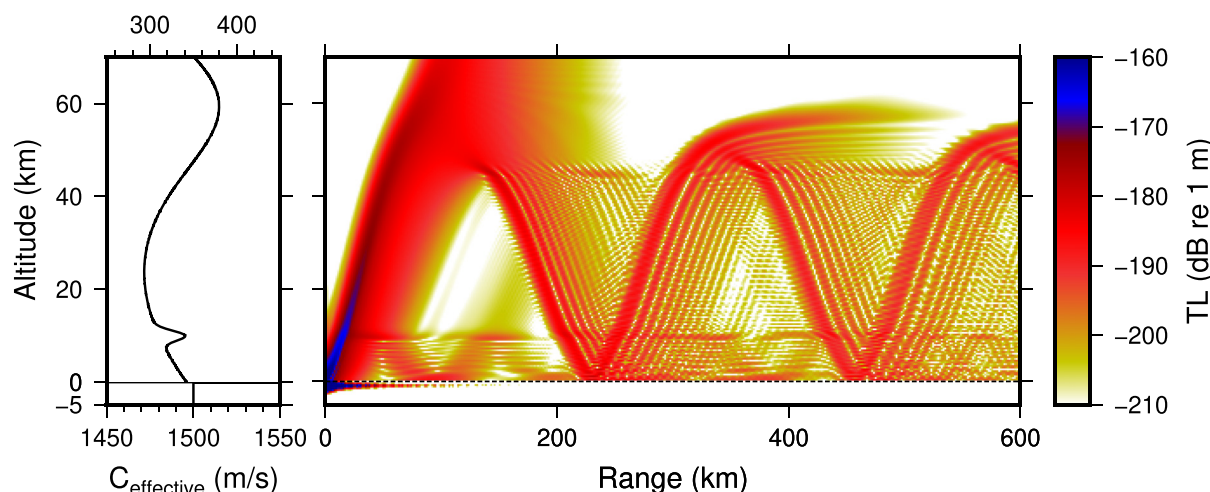

FIG. 1. (Color online) Infrasound propagation from an underwater source at a depth of 500 m and a 0.5 Hz source.

J. Acoust. Soc. Am. **147** (2), February 2020

Averbuch *et al.* 1067

investigated. The FFP[34] is used to simulate the acoustic pressure in the atmosphere from a submerged source at different depths and with different strengths. It provides an exact solution for wave propagation in a 2 D horizontally layered media in the (f)–(k) domain by solving the continuity equations for all interfaces. These equations comprise the continuity of normal stress (pressure) and vertical displacement. The explicit treatment of the boundary conditions allows handling variations in speed of sound and density profiles as well as stark discontinuities, such as the ocean-atmosphere interface, without numerical approximations (unlike finite-difference discretization). Both media are divided into 20 m homogeneous layers, and each layer is attributed with speed of sound and density values that

correspond to the layer altitude. Atmospheric winds are integrated by the effective sound speed approximation, C_{eff}, which is defined as the sum of the adiabatic speed of sound and the wind component in the direction of propagation.[35] The source is set to a monopole volume injection, and the Fast Fourier Transform is used to reconstruct the frequency space pressure field.

Figure 1 shows the transmission loss of eastward propagation (90 degrees) in the atmosphere for a 0.5 Hz source at a depth of 500 m. The atmospheric profile consists of tropospheric and stratospheric waveguides at 10 and 50 km, respectively, and the depth of the oceanic layer is five kilometers. The simulated trace velocities, which indicates the wavenumbers, range from 300 m/s to 450 m/s and is kept fixed through
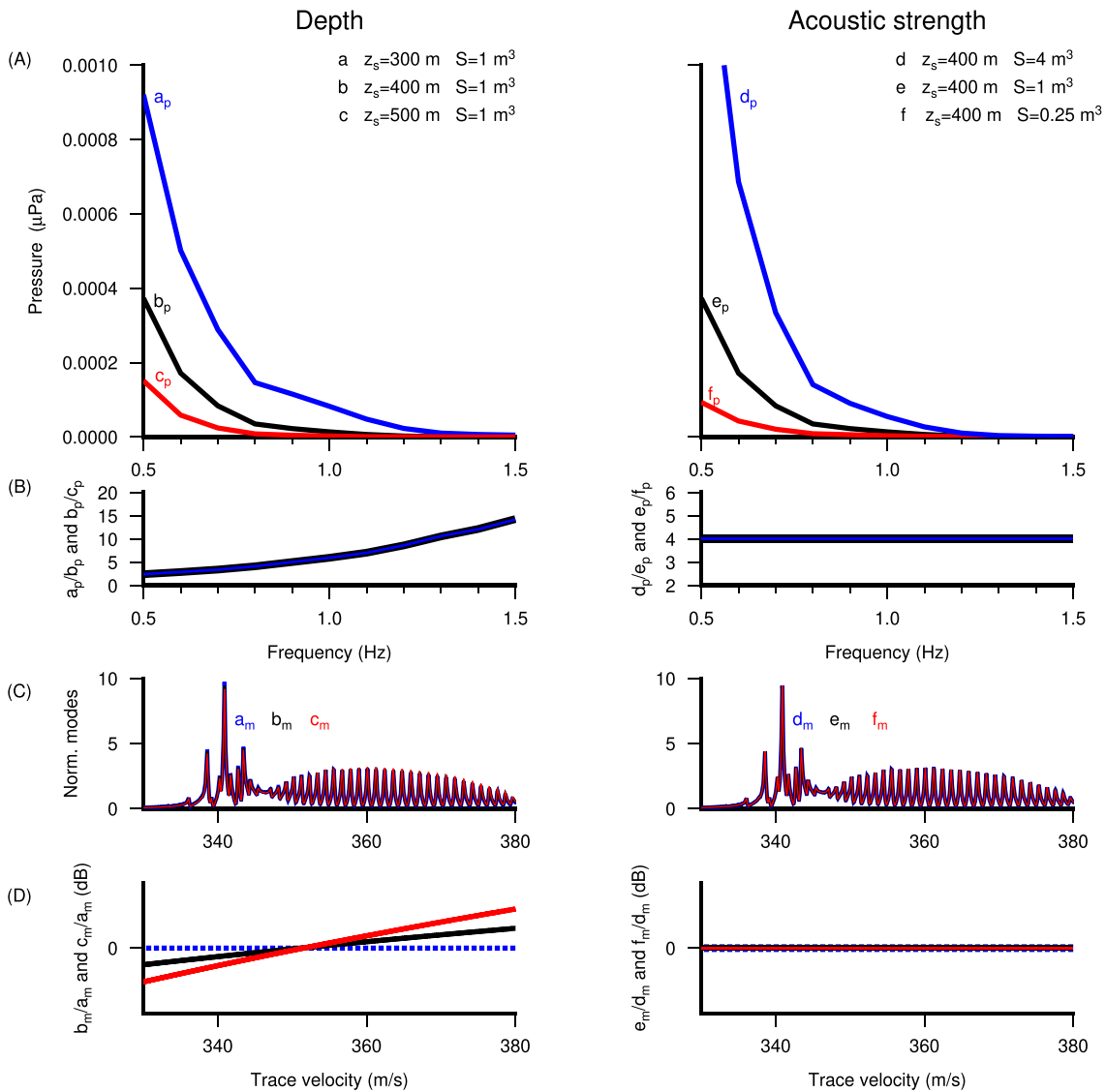

FIG. 2. (Color online) Changes in the atmospheric pressure perturbations due to variations in the source parameters. The left column shows the effect of the source depth on the simulated pressure, and the right column shows the effect of the source strength on the simulated pressure. Subscripts p and m correspond to pressure and normalized modes by RMS, respectively. Row (A) shows atmospheric discrete frequency pressure curves 300 km from the source for different source parameters. Row (B) shows the ratios of the curves in the upper frames [e.g., the pressure of curve (a) for 1 Hz divided by the pressure of curve (b) for the same frequency]. Row (C) shows the normalized, propagating modes for a 0.5 Hz source, and row (D) shows the ratio of the normalized modes (relative to the red curve).

the remainder of this study. Due to the low-frequency contents of the source, the interface becomes transparent to the evanescent waves, allowing it to get trapped in both waveguides and efficiently propagate over vast distances. For this atmospheric profile, the tropospheric waveguide encompasses low trace velocity modes (<345 m/s), and the stratospheric waveguide encompasses high trace velocity modes.

The effects due to variations of the source depth and strength on the atmospheric perturbations are demonstrated in Fig. 2. Although different source parameters may yield similar pressure curves [row (A), blue and red lines], the ratios of the curves (a/b, b/c, d/e, and e/f) within each set are different [row (B)]. There is a linear relation for the source strength and a non-linear relation for the source depth. Row (C) shows the normalized modes, at $z = 0$ m, for a 0.5 Hz source. An increase in the source depth leads to a relative decrease in the lower trace velocity amplitudes compared to the higher trace velocity amplitudes. This behavior is further emphasized by the ratios of normalized modes in row (D). Such variations imply that the radiation pattern in the atmosphere depends on the source depth. In contrast, there are no variations in the normalized modes due to changes in the source strength. This means that a linear scalar, such as strength, cannot adequately compensate for a different source depth. Therefore, the use of infrasonic signals to distinguish between different underwater source parameters is feasible.

The linear effect of the source strength in Fig. 2 is a direct consequence of the linear FFP model. However, the non-linear impact of the variation in the source depth is less intuitive. Let us define v and v_{tr} as the medium's acoustic velocity and modeled trace velocity, respectively. The corresponding medium's wavenumber is $k = 2\pi f/v$, horizontal wavenumber is $k_r = 2\pi f/v_{tr}$, and vertical wavenumber is $k_z = 2\pi f \sqrt{1/v^2 - 1/v_{tr}^2}$. Propagation between the source to the ocean-atmosphere interface is proportional to $A e^{ik_z z} e^{ik_r r}$. Assuming that the coupling is predominantly due to inhomogeneous waves ($v_{tr} < v$), $k_z = i\hat{k}_z$, and the source-to-interface propagation can be written as $A e^{-\hat{k}_z z} e^{ik_r r}$. The function $e^{-\hat{k}_z z}$ is a real decaying function, and it explains the non-linear relation due to variations in the source depth [Fig. 2, rows (A) and (B)]. Also, different trace velocities correspond to different vertical wavenumbers $\hat{k}_z$. As a result, for a fixed frequency, the decay rate of the modeled trace velocities differs from one to another, leading to variations in the radiation pattern in the atmosphere due to changes in the source depth [Fig. 2, rows (C) and (D)].

Bayesian inversions are used in a wide range of physical problems when a parameter space needs to be evaluated from a set of observations.[28] It provides a rigorous probabilistic framework that combines *a priori* knowledge on the parameter space and a set of observations into a posterior probability distribution as a function of the free parameters. Here, a probabilistic Bayesian inversion scheme is used to estimate the source parameters from a set of observed signals. The Bayesian formulation of our original question is $P(z_s, S|\boldsymbol{M})$, where P is the probability density function.

A synthetic dataset, $m(z_s, r_i, \theta_j, \omega_k, S)$, of the acoustic pressure perturbation on ground level ($z = 0$ m) is generated by the FFP for a range of source depths, z_s, ranges, r_i, directions of propagation, θ_j, frequencies, ω_k, and source strengths, S. The motivation to use discrete frequencies and not absolute travel times, as in seismology, is purely due to numerical costs. Due to the stark contrast of densities and acoustic velocities, fast methods to compute travel times, like ray tracing, cannot be used. Therefore, in order to obtain travel times from an underwater source, one must use a full-wave model either in the time domain or compute it for a large number of frequencies in the frequency domain. These simulations are numerically expensive. It will be shown that accurate results can be obtained by using a selection of discrete frequencies and avoiding simulating an entire time series. Moreover, higher accuracy can be easily obtained by adding more frequencies with a low numerical cost.

After choosing certain values for the source depth and strength, the observations, $M(r_i, \theta_j, \omega_k)$, are obtained by adding noise to the synthetic data as follows:

$$M(r_i, \theta_j, \omega_k) = m(z_s, r_i, \theta_j, \omega_k, S) + \mathrm{N},$$
$$\mathrm{N} \sim \mathcal{N}(\mu = 0, \sigma^2(\mathrm{SNR})), \tag{1}$$

where N is a randomly added noise from a normal distribution with a zero mean (μ) and a variance (σ) that is defined by the SNR.

In order to calculate the Bayesian probability of a given z_s and S, their probability distributions, $p(z_s)$ and $p(S)$, and the variance of the cost function need to be evaluated. $p(z_s)$ and $p(S)$ are assumed to be piecewise constant functions defined as

$$p(z_s) = \begin{cases} \dfrac{1}{(z_{max} - z_{min})/dz} & z_{min} < z < z_{max} \\ 0 & \text{elsewhere,} \end{cases}$$
$$p(S) = \begin{cases} \dfrac{1}{(S_{max} - S_{min})/dS} & S_{min} < S < S_{max} \\ 0 & \text{elsewhere.} \end{cases} \tag{2}$$

Here, z_{min}, z_{max}, S_{min}, and S_{max} represent the boundaries of the searching range. Their corresponding increments are dz and dS. Equation (2) means that the occurrence probabilities of the parameters within the searching range are equal. The variance of the cost function, $\sigma(r_i, \theta_j, \omega_k)$, is the same variance defined by the SNR in Eq. (1). In practice, this assumption is valid since SNR values are evaluated continuously as part of the data analysis.[36,37]

Given a set of observations $M(r_i, \theta_j, \omega_k)$ and synthetic dataset $m(z_s, r_i, \theta_j, \omega_k, S)$, the probability that a source was in a certain depth z_s and strength S is

J. Acoust. Soc. Am. **147** (2), February 2020

Averbuch *et al.* 1069

$$P(z_s, S | M(\boldsymbol{r}, \boldsymbol{\theta}, \boldsymbol{\omega})) = \frac{p(z_s)p(S)e^{-\sum_{i,j,k}\left(1/2\sigma(r_i,\theta_j,\omega_k)^2\right)\|M(r_i,\theta_j,\omega_k)-m(z_s,r_i,\theta_j,\omega_k,S)\|^2}}{\int_{S_{min}}^{S_{max}}\int_{z_{min}}^{z_{max}} p(z)p(S)e^{-\sum_{i,j,k}\left(1/2\sigma(r_i,\theta_j,\omega_k)^2\right)\|M(r_i,\theta_j,\omega_k)-m(z_s,r_i,\theta_j,\omega_k,S)\|^2}\,dzdS}. \tag{3}$$

This posterior probability is calculated for each possible combination of source depths and strengths. The integration of the likelihood function over the entire search range, as in the denominator, acts as a normalization function. It ensures that the sum over all probabilities will be unity. The trapezoidal rule is used to evaluate the double integral.

The accuracy of the inversion is tested under the variation of the number of stations, source depth, frequency range (number of discrete frequencies), and SNRs. The experiment starts with a broad station coverage, where the effect of the frequency band is investigated. Then, the number of stations is reduced until attaining a one-station inversion. For this part, a known atmospheric profile is used. Finally, the influence of atmospheric uncertainty is tested by using an ensemble of 25 realistic perturbed atmospheric profiles provided by the European Center for Medium-Range Weather Forecasts (ECMWF).

III. RESULTS

A. Number of stations vs frequencies

Here, we estimate the effects of the number of stations, frequency range, and SNR on the inversion results. In order to reduce the uncertainties of the problem, a known, smooth atmospheric profile is used. The idealized profile consists of a tropospheric (10 km) and a stratospheric (50 km) duct with varying strength as a function of the propagation azimuth. Defining zero degrees as the north, the strengths of the ducts increase easterly. Table I shows the modeling parameters used for generating the data, and the search ranges in the inversion scheme were set to all of the modeled depths and strengths. The parameters dz, $d\theta$, df, and dS represent the increment sizes within the ranges z, θ, f, and S, respectively.

To demonstrate the feasibility of the inversion, a ten-station, and ten-frequency inversion is used (the position of the stations is shown in Appendix A). From each azimuth of propagation, two ranges were chosen according to the atmospheric ducts to ensure that signals arrive at all stations. The calculated probabilities for the different source depths are presented in Fig. 3. Besides one inversion (SNR = 1 for $z_s = 1200$ m), all of the inversion results provided accurate

results for the source depth. As the SNR decreases, the uncertainty of the source depth increases. However, it is always bounded within a ±60 m range. Most of the source strength estimations are within a range of ±0.05 m^3, which is less than a 5% error. This small deviation can be attributed to the randomly added noise. For SNR = 1, the uncertainty of the depth and strength increases, and a depth-yield trade-off relation appears in a ridge-like form. Throughout this section, the observation's source parameters are set to $z_s = 1000$ m, and $S = 1$ m^3.

Statistics from 1000 realizations are used to estimate the impact of the number of frequencies, number of stations, and SNRs on the inversion results. The observations are set according to Eq. (1), and the source parameters with the highest probability are extracted. The first inversion test is set to estimate the effect of the frequency range. Figure 4 shows the distribution of the 1000 source parameters from a ten-station inversion for a single (discrete) frequency. For the source depth, the medians are either accurate or very close to its real value, and the 25th and 75th percentiles are bounded between 20 m and 100 m from it. Medians of the source strength provide a good estimation as well. However, there is a distinct skewness of the source strength distribution around its median, and the 25th and 75th percentiles are bounded between 0.5m^3 and 2.7m^3 from it. Results from the combined three-frequency inversions accurately resolve both depth and strength for all SNRs while minimizing the variance range. Table III in Appendix B contain the number of outliers presented in Fig. 4.

Using multiple frequencies provides more constraints for the inversion, therefore, improving the accuracy as well as reducing their variance. Acquiring more discrete frequencies depends only on the signal and its sampling rate. However, recordings from multiple stations are not always available. Results of ten frequencies and ten-, five-, and single-station inversions show almost no difference in the estimated depth (Fig. 5). Nevertheless, the approximated source strength is sensitive to the number of stations and SNRs. The variance of the one station inversion increases with the decrease of SNR, and the peaky distributions of the higher SNRs lead to a high number of outliers (Table IV in Appendix B).

B. Atmospheric uncertainties using an ECMWF ensemble

An exact atmospheric profile, as in Sec. III A, provides robust inversion results given a different number of stations and SNRs. However, the actual state of the atmosphere is

TABLE I. Modeling parameters for the smooth atmospheric profiles.

z [m]	dz [m]	θ [deg]	$d\theta$ [deg]	f [Hz]	df [Hz]	S [m^3]	dS [m^3]
200–1000	20	10–90	20	0.5–1.5	0.1	0.2–3	0.002

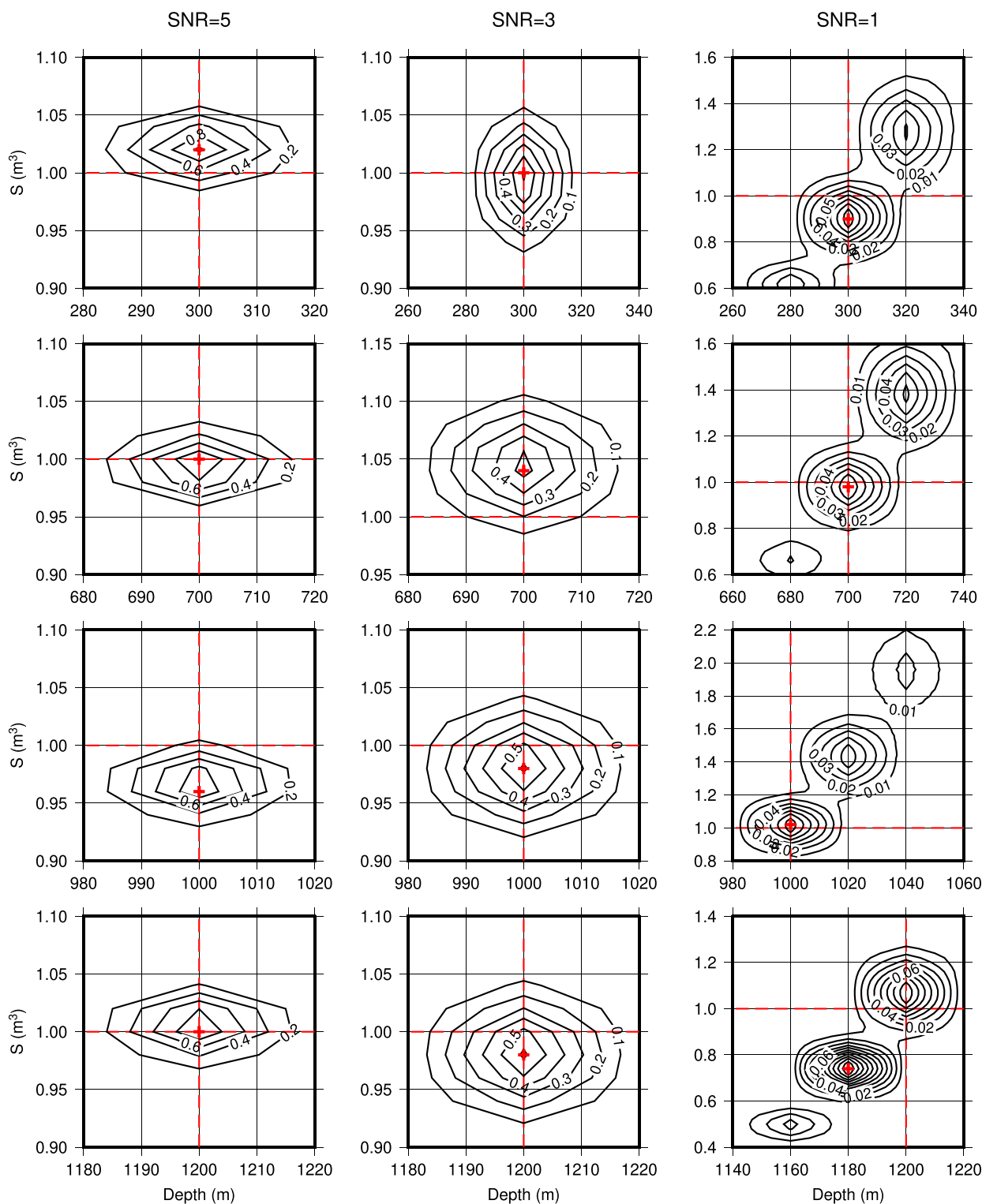1070   J. Acoust. Soc. Am. **147** (2), February 2020

Averbuch *et al.*

FIG. 3. (Color online) Inversion results using ten stations and ten frequencies. The red lines correspond to the real source depth and strength, and the contour lines provide the probabilities. (a) For SNR = 5, the inversion results are correct, and the probability is high. (b) SNR = 3 leads to overestimating the source strength. The source depth is correct. (c) SNR = 1 leads to higher uncertainties in both depth and strength. Moreover, the probabilities are one order of magnitude lower than in (a) and (b).

estimated by an atmospheric model and a data assimilation system, which is never exact. The atmospheric properties can differ from the real atmosphere due to both model and observation uncertainties. To study the influence of the atmospheric uncertainties on the accuracy of the inversion, we apply

probabilistic infrasound propagation modeling using an ensemble of realistic perturbed atmospheric profiles.[38]

Realistic perturbed atmospheric profiles are provided by the Ensemble Data Assimilation (EDA) system of the ECMWF. The EDA consists of 25 members that discretely

J. Acoust. Soc. Am. **147** (2), February 2020
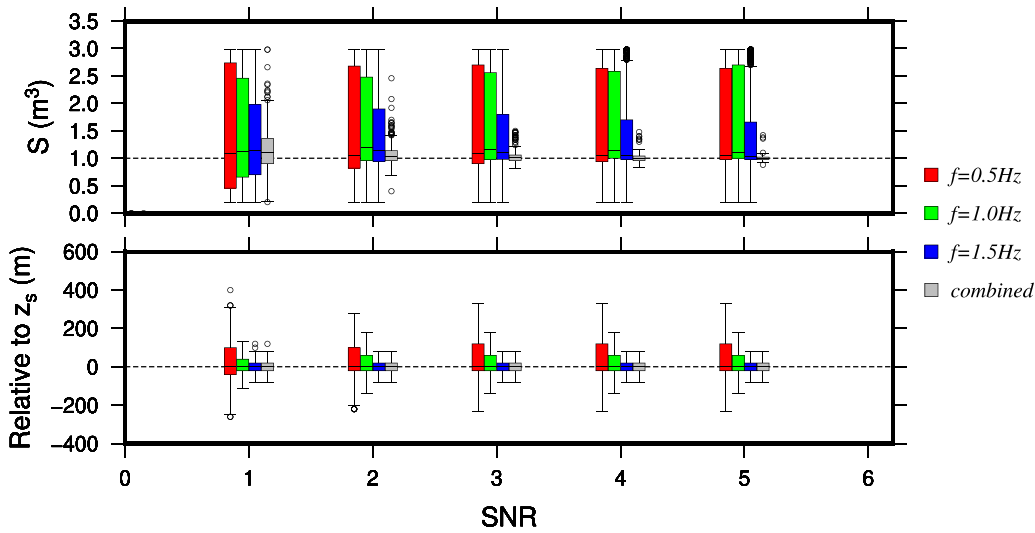
Averbuch *et al.*   1071

FIG. 4. (Color online) Result distributions of 1000 realizations for varying SNR. The boxes represent the 25th and 75th percentile range, and the bars the 5th, 50th, and 95th percentiles. The circles represent outliers. The red, green, and blue colors are ten-station single-frequency inversions. Gray boxes represent the ten-station and three-frequency inversions results.

sample the probability density function of the atmosphere.[39,40] The EDA mean is defined as the "real" atmosphere, and used to generate the "observations," while the individual EDA members are used to create 25 synthetic, but likely, datasets for the inversion. For each of the data sets, the source parameter probabilities are calculated and eventually combined into one posterior probability distribution that captures the effect of the atmospheric uncertainties. Therefore, the final posterior probability, $\bar{P}(z_s, S|M(\boldsymbol{r}, \boldsymbol{\theta}, \boldsymbol{\omega})$, will be

$$\bar{P}(z_s, S|M(\boldsymbol{r}, \boldsymbol{\theta}, \boldsymbol{\omega})) = \frac{1}{N} \sum_{l=1}^{N} P_l(z_s, S|M(\boldsymbol{r}, \boldsymbol{\theta}, \boldsymbol{\omega})), \quad (4)$$

when N is the number of the ensemble members, and $P_l(z_s, S|M(\boldsymbol{r}, \boldsymbol{\theta}, \boldsymbol{\omega}))$ is the posterior probability for the inversion with the lth member.

Unlike the homogeneous water layer that is used in Sec. III A, now, the atmospheric profiles are placed on top of a typical oceanic profile known as the Munk profile.[41] This oceanic profile consists of a minimum in the speed of sound profile around a depth of 1000 m, which forms the Sound Fixing and Ranging channel. Defining the EDA mean as the "real" atmospheric conditions, an "observation" dataset, $M(r_i, \theta_j, \omega_k)$, is generated for a source at $z = 1000$ m and $S = 1$ m^3. Then, a synthetic dataset, $m_l(z_s, r_i, \theta_j, \omega_k, S)$, is generated for each ensemble member according to the parameters in Table II. Figure 6 shows the simulated
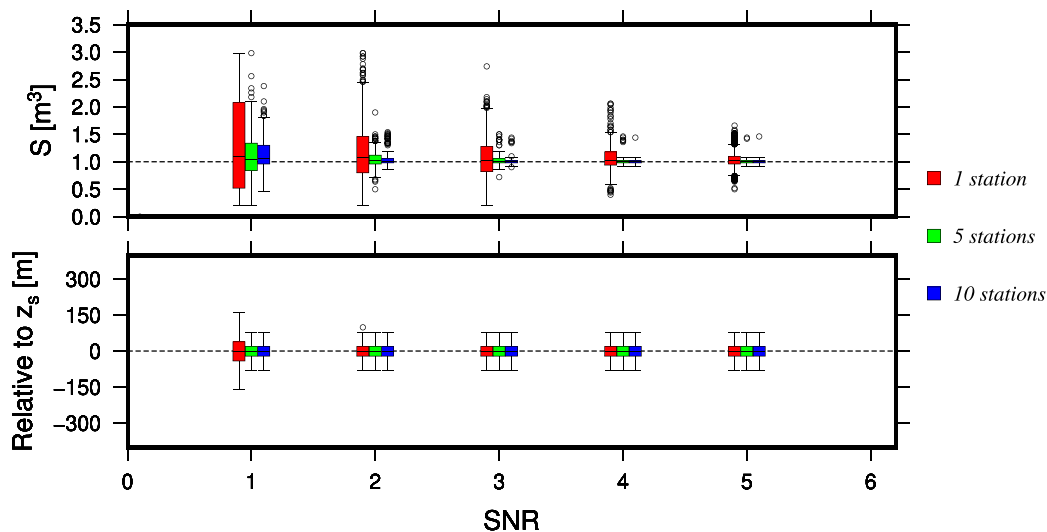

FIG. 5. (Color online) Results distributions of 1000 ten-frequency inversions with a different number of stations. The blue, green, and red boxes represent the ten-station, five-station, and one-station inversions, respectively.

TABLE II. ECMWF modeling parameters.

z [m]	dz [m]	θ [deg]	$d\theta$ [deg]	f [Hz]	df [Hz]	S [m^3]	dS [m^3]
500–1500	20	70–110	20	0.5–1.5	0.1	0.2–3	0.02

absolute pressure curves on the ground ($z = 0$ m) from a 0.8 Hz source at a depth of 1000 m, for the 25 ensemble members (gray) and the EDA mean (black). The variation in the pressure curves is associated with the variance of the profiles (Fig. 6 left column). Small variations in the ducts' altitude lead to different spatial maxima positions. For example, the absolute pressure at 290 km for $\theta = 70°$ ranges between approximately 0 μPa and 0.009 μPa, while for $\theta = 90°$ at 280 km, it ranges between 0.0005 μPa and 0.0055 μPa. Moreover, inspecting the propagation for $\theta = 110°$ shows that the absolute pressure at 160 km ranges between 0.005 μPa and 0.01 μPa, and between approximately 0 μPa and 0.007 μPa at 300 km. Due to such differences, the positions of the receivers will have a significant role in the inversion results.

The inversion performance is tested on four different setups (Fig. 7). Two-station inversion is performed for three location pairs along propagation paths in three azimuths. The fourth test is a one-station inversion. Receiver locations are picked according to the return height of the ducts to guarantee

the arrival of atmospheric phases at the sites. However, the absolute pressure range at the locations varies in order to capture the atmospheric uncertainties effect. For instance, there is a 0.005 μPa and 0.009 μPa range at $R_{110°} = 160$ km and $R_{70°} = 290$ km, respectively. These ranges correspond to the station locations for inversions (a)–(c), and (g)–(i) in Fig. 7.

Figure 7 shows the inversion results for the four setups (rows), and three SNRs (columns). Regardless of the inversion setup and SNR, all of the approximated source depths are bounded between 900 m and 1100 m. Inversions (a) and (d) have the most significant uncertainties in the source depth, while inversions (b) and (c) are bounded between 950 m and 1050 m. The effect of the absolute pressure range at the sites is prominent in the source strength estimations. Inversions (a) underestimate the source strength to half of its real value, as well as having low probabilities. In contrast, inversions (c) estimate it to be 0.9 m^3 with relatively high probabilities. Finally, the one station inversions (d) perform better than the two station inversions (a). The large variance in the propagation in 70° impairs the capability to resolve the source parameters accurately.

IV. CONCLUSIONS AND DISCUSSION

This work studied the prospect of using long-range infrasound signals from submerged sources to invert for the
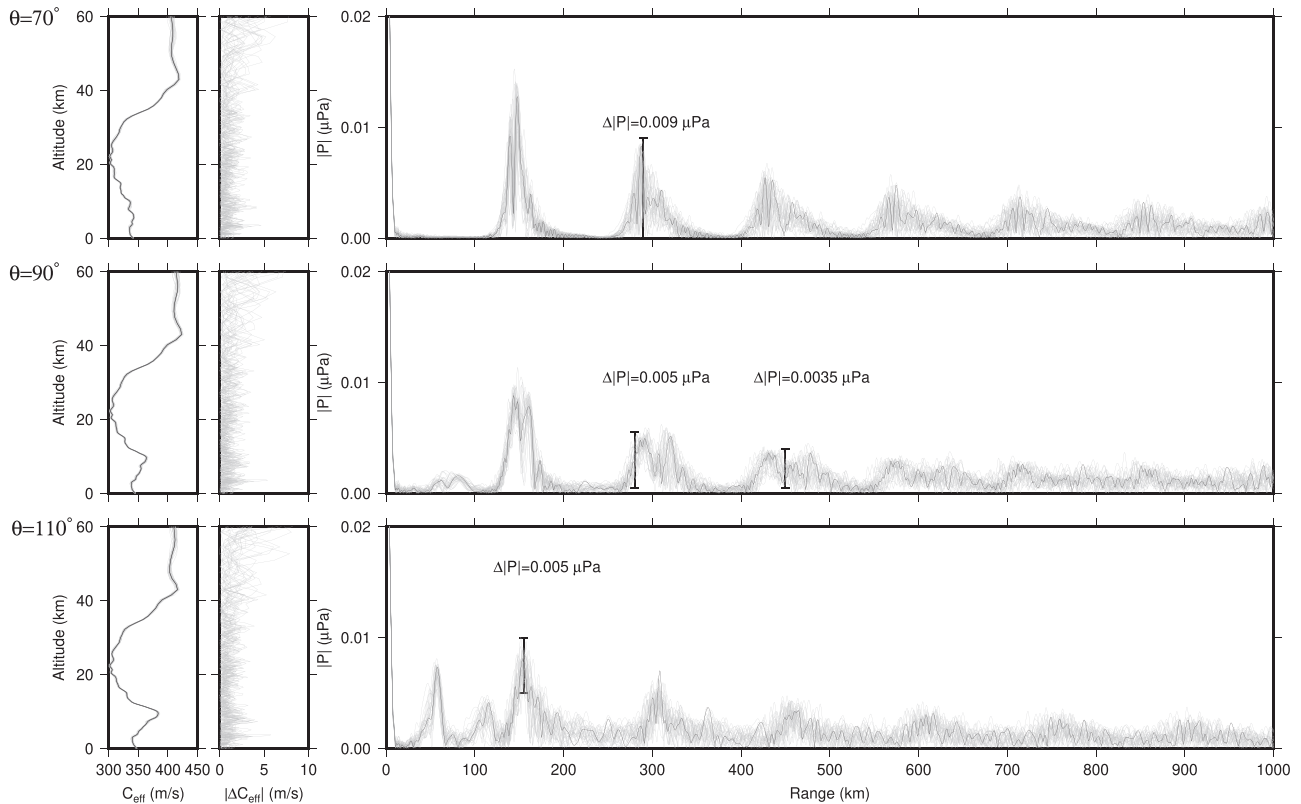

FIG. 6. Simulated absolute pressure curves on the ground ($z = 0$ m) from a 0.8 Hz source at a depth of 800 m, for the 25 ensemble members (gray) and the EDA mean (black). The left frames show the effective sound speed profiles for each propagation azimuth, and the absolute difference of each ensemble member from the EDA mean. The bars in the absolute pressure frames indicate the absolute pressure range in three of the locations of the receivers.
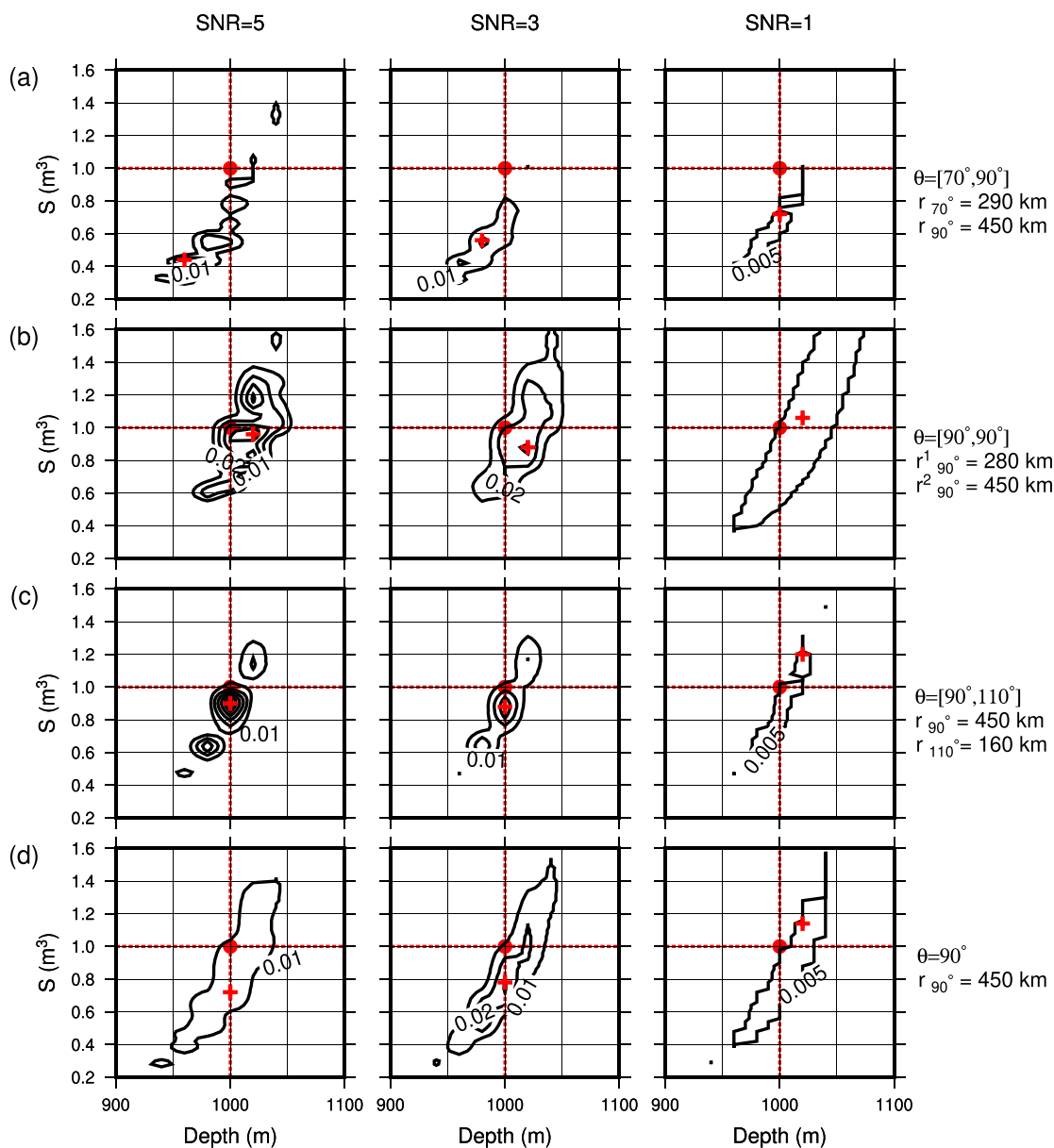
FIG. 7. (Color online) Probabilities for different inversions' setups. The number of stations and their locations is indicated on the right-hand side of each row. The columns indicate the SNR. Red lines indicate the real source parameters, and red crosses indicate the parameters with the highest probability.

source depth and strength. A probabilistic inversion scheme was tested on two synthetic case studies and showed that using long-range infrasound signals to resolve the depth and strength of a shallow submerged source is attainable. Although the analysis focuses on underwater sources, the results can be useful also for subsurface sources.

The inversion is based on minimizing the difference between an observable and modeled signal and provides a posterior probability density function for the parameter space. In the first synthetic case, a known atmospheric profile is used to evaluate the effect of the number of stations, the signals' frequency band, and SNR on the inversion results (Sec. III A). It is shown that broadband signals are essential for resolving the source parameters. The

sensitivity of the coupling mechanisms to different frequency bands set stringent constraints on the inversion, allowing an accurate estimation of the source depth and strength even for low SNRs. The skewness of the source depth and strength distribution of Fig. 4 can be a result of the linear and non-linear effects due to variations in the source parameters. Variations in the source depth can lead to significant variations in amplitude with a stronger effect for decreasing depth (i.e., a small decrease in the source depth lead to a large increase in the received signal's amplitude). Therefore, it seems that fine-tuning of the source parameters for minimizing the likelihood function can be easily achieved by a small increase of the source depth and larger variations of the source strength. Note that

this behavior exists only in the single-frequency inversions, and multiple frequencies provide a symmetric distribution around the real source parameters.

There was no difference between the five- and ten-station inversion. However, comparing one- and five-station inversion results show that multiple stations reduce the depth-yield trade-off. This behavior is further seen in the comparison between one- and two-station inversion in Sec. III B. Results from Sec. III A indicate that using a broader frequency range is more beneficial than multiple station inversion. A significant increase in/of the frequency range will allow obtainment of the space-time representation of the simulated wavefield. In such a case, arrival times of the different atmospheric phases can further constrain the inversion.

An ensemble of perturbed atmospheric profiles by the ECMWF is used to appraise the effect of atmospheric uncertainties on the inversion results. Propagation in three different azimuths experiencing different speed-of-sound profiles provided us with versatile datasets to choose the location of the stations. Results show that the spatial position of the stations is crucial to the accuracy of the estimated source parameters. The large variance of the pressure at $\theta = 70°$, compared to the stations at $\theta = 90°$ and $\theta = 110°$, leads to underestimating the source strength by approximately 50%. Moreover, inversions (a) perform worse than the one station inversions (d), which may seem like a contradiction of our previous statement that higher spatial coverage improves the results. While in this case it is true, one must keep in mind that the quality of the data plays an essential role in the inversion. Naturally, inversion with a small variance dataset performs better than with a large variance dataset. Yet, regardless of the number of stations, their positions, and SNRs, all of the estimated depths were within a ± 100 m range from the real source depth. Variations up to 5 m/s in the ensemble effective speed of sound profiles proved to have a significant impact on the narrowband simulated pressure. This behavior motivates the incorporation of narrowband acoustic simulations in inversions for atmospheric specifications.

Throughout this study, the source type was kept as a monopole in order to limit the number of unknown parameters. Different source types will have a different radiation pattern, and whether one can invert also for the source type is still unknown. Another behavior that was excluded from this study is the non-linearity in the vicinity of the source. Although it is known that explosions are non-linear in the near-field, to the best of our knowledge, its effect on the transmission through stark interfaces has not been studied. In addition, no constraints or prior knowledge on the source parameters were used. Therefore, any restrictions on the source parameters will improve the accuracy of the estimated parameters.

Implications regarding shallow underground sources can be deduced on the basis of this study. However, benchmark tests with real events should be the scope of future research. Moreover, this study assumes a horizontally stratified range-independent medium. Therefore, further study on the effect of a complex environment, such as topography and a range-dependent medium, on the inversion results is needed.

ACKNOWLEDGMENTS

APPENDIX A: STATIONS POSITION

Figure 8 shows the lateral position of the stations, and the absolute pressure curves for propagation in the stations directions.
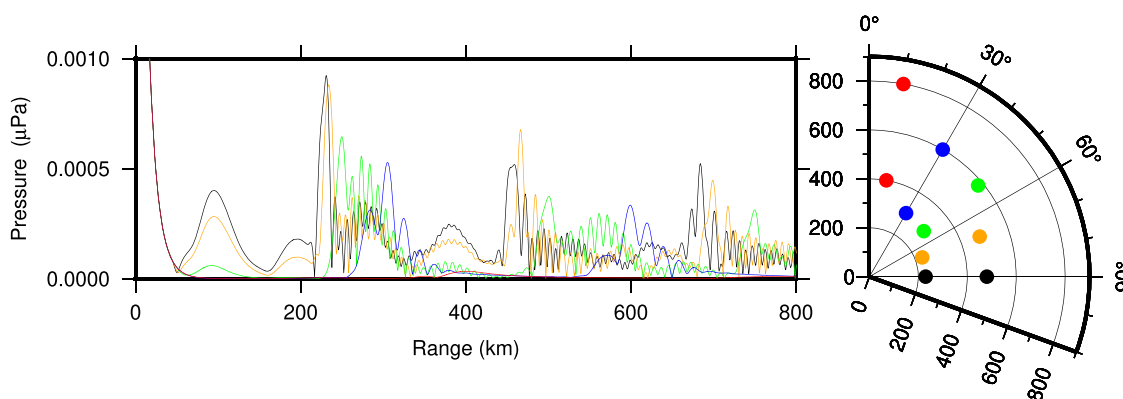

FIG. 8. (Color online) Lateral position of the stations, and the corresponding absolute pressure curves from a 0.5 Hz source at a depth of 500 m. The colors of the curves correspond to the colors of the stations.

APPENDIX B: NUMBER OF OUTLIERS

The following Tables III and IV show the number of outliers for each set up that is presented in Figs. 4 and 5.

TABLE III. Number of outliers for each setup in Fig. 4.

SNR	1				2				3				4				5			
	f_1	f_2	f_3	comb	f_1	f_2	f_3	comb	f_1	f_2	f_3	comb	f_1	f_2	f_3	comb	f_1	f_2	f_3	comb
outliers S	—	—	—	58	—	—	—	107	—	—	—	104	—	—	74	35	—	—	98	25
outliers Z_s	5	4	2	2	12	—	—	—	1	—	—	—	—	—	—	—	—	—	—	—

TABLE IV. Number of outliers for each setup in Fig. 5.

SNR	1			2			3			4			5		
Num. of stations	1	5	10	1	5	10	1	5	10	1	5	10	1	5	10
outliers S	—	44	44	34	172	127	24	122	39	51	65	8	274	27	3
outliers Z_s	—	—	—	1	—	—	—	—	—	—	—	—	—	—	—

[1] J. A. Sharpe, "The production of elastic waves by explosion pressures. I. Theory and empirical field observations," Geophysics 7, 144–154 (1942).

[2] J. A. Sharpe, "The production of elastic waves by explosion pressures. II. Results of observations near an exploding charge," Geophysics 7, 311–321 (1942).

[3] E. W. Carpenter, "Teleseismic signals calculated for underground, underwater, and atmospheric explosions," Geophysics 32, 17–32 (1967).

[4] M. Holt, "Underwater explosions," annual report (1977), pp. 187–214, www.annualreviews.org.

[5] G. C. Werth and R. F. Herbst, "Comparison of amplitudes of seismic waves from nuclear explosions in four mediums," J. Geophys. Res. 68, 1463–1475, https://doi.org/10.1029/JZ068i005p01463 (1963).

[6] R. A. Mueller and J. R. Murphy, "Seismic characteristics of underground nuclear detonations: Part I. Seismic spectrum scaling," B. Seismol. Soc. Am. 61, 1675–1692 (1971).

[7] R. A. Mueller and J. R. Murphy, "Seismic characteristics of underground nuclear detonations: Part II. Elastic energy and magnitude determinations," J. Geol. 61, 1693–1704 (1971).

[8] A. Douglas, D. J. Corbishley, C. Blamey, and P. D. Marshall, "Estimating the firing depth of underground explosions," Nature 237, 26–28 (1972).

[9] L. R. Sykes and G. C. Wiggins, "Yields of Soviet underground nuclear explosions at Novaya Zemlya, 1964–1976, from seismic body and surface waves," in Proceedings of the National Academy of Sciences of the United States of America (1986), Vol. 83, pp. 201–205.

[10] A. L. Kafka, "Rg as a depth discriminant for earthquakes and explosions: A case study in New England," B. Seismol. Soc. Am. 80, 373–394 (1990).

[11] W.-Y. Kim, D. W. Simpson, and P. G. Richards, "Discrimination of earthquakes and explosions in the eastern United States using regional high-frequency data," Geophys. Res. Lett. 20, 1507–1510, https://doi.org/10.1029/93GL01267 (1993).

[12] W. R. Walter, K. M. Mayeda, and H. J. Patton, "Phase and spectral ratio discrimination between NTS earthquakes and explosions. Part I: Empirical observations," B. Seismol. Soc. Am. 85, 1050–1067 (1995).

[13] D. C. Bowman, "Yield and emplacement depth effects on acoustic signals from buried explosions in hard rock," B. Seismol. Soc. Am. 109(3), 944–958 (2019).

[14] E. Rougier, H. J. Patton, E. E. Knight, and C. R. Bradley, "Constraints on burial depth and yield of the 25 May 2009 North Korean test from hydrodynamic simulations in a granite medium," Geophys. Res. Lett. 38, L16316, https://doi.org/10.1029/2011GL048269 (2011).

[15] H. Benioff, M. Ewing, and F. Press, "Sound waves in the atmosphere generated by a small earthquake," in Proceedings of the National Academy of Sciences of the United States of America (1951) Vol. 37, pp. 600–603.

[16] W. L. Donn and E. S. Posmentier, "Ground-coupled air waves from the Great Alaskan Earthquake," J. Geophys. Res. 69, 5357–5361, https://doi.org/10.1029/JZ069i024p05357 (1964).

[17] S. Watada, T. Kunugi, K. Hirata, H. Sugioka, K. Nishida, S. Sekiguchi, J. Oikawa, Y. Tsuji, and H. Kanamori, "Atmospheric pressure change associated with the 2003 Tokachi-Oki earthquake," Geophys. Res. Lett. 33(24), L24306, https://doi.org/10.1029/2006GL027967 (2006).

[18] L. G. Evers, "Evanescent Wave Coupling in a Geophysical System," in AGU Fall Meeting Abstracts (2014) Vol. 1, p. 3871.

[19] J. D. Assink, G. Averbuch, P. S. M. Smets, and L. G. Evers, "On the infrasound detected from the 2013 and 2016 DPRK's underground nuclear tests," Geophys. Res. Lett. 43, 3526–3533, https://doi.org/10.1002/2016GL068497 (2016).

[20] S. Shani-Kadmiel, J. D. Assink, P. S. M. Smets, and L. G. Evers, "Seismoacoustic coupled signals from earthquakes in central Italy: Epicentral and secondary sources of infrasound," Geophys. Res. Lett. 45, 427–435, https://doi.org/10.1002/2017GL076125 (2018).

[21] J. Assink, G. Averbuch, S. Shani-Kadmiel, P. Smets, and L. Evers, "A seismo-acoustic analysis of the 2017 North Korean nuclear test," Seismol. Res. Lett. 89, 2025–2033 (2018).

[22] P. Campus and D. R. Christie, "Worldwide observations of infrasonic waves," in Infrasound Monitoring for Atmospheric Studies (Springer, Dordrecht, The Netherlands, 2009), pp. 185–234.

[23] O. A. Godin, "Anomalous transparency of water-air interface for low-frequency sound," Phys. Rev. Lett. 97(16), 164301 (2006).

[24] B. E. McDonald and D. C. Calvo, "Enhanced sound transmission from water to air at low frequencies," J. Acoust. Soc. Am. 122(6), 3159–3161 (2007).

[25] O. A. Godin, "Low-frequency sound transmission through a gas-solid interface," J. Acoust. Soc. Am. 129, EL45–EL51 (2011).

[26] M. A. Biot, "The interaction of Rayleigh and Stoneley waves in the ocean bottom*," B. Seismol. Soc. Am. 42, 81–93 (1952).

[27] J. G. Scholte, "The range of existence of Rayleigh and Stoneley waves," Geophys. J. Int. 5, 120–126 (1947).

[28] A. Tarantola, Inverse Problem Theory and Methods for Model Parameter Estimation (Society for Industrial and Applied Mathematics, Philadelphia, Pennsylvania, 2005).

[29] J. Tromp, C. Tape, and Q. Liu, "Seismic tomography, adjoint methods, time reversal and banana-doughnut kernels," Geophys. J. Int. 160, 195–216 (2005).

[30] S. Maranò, C. Reller, H.-A. Loeliger, and D. Fäh, "Seismic waves estimation and wavefield decomposition: Application to ambient vibrations," Geophys. J. Int. 191, 175–188 (2012).

[31] K. Kim and A. Rodgers, "Waveform inversion of acoustic waves for explosion yield estimation," Geophys. Res. Lett. 43(13), 6883–6890, https://doi.org/10.1002/2016GL069624 (2016).

[32]J.-M. Lalande, O. Sèbe, M. Landès, P. Blanc-Benon, R. S. Matoza, A. Le Pichon, and E. Blanc, "Infrasound data inversion for atmospheric sounding," Geophys. J. Int. **190**, 687–701 (2012).

[33]J. D. Assink, R. Waxler, W. G. Frazier, and J. Lonzaga, "The estimation of upper atmospheric wind model updates from infrasound data," J. Geophys. Res. Atmos. **118**, 10707–10724, https://doi.org/10.1002/jgrd.50833 (2013).

[34]H. Schmidt and G. Tango, "Efficient global matrix approach to the computation of synthetic seismograms," Geophys. J. Roy. Astr. S. **84**(2), 331–359 (1986).

[35]O. A. Godin, "An effective quiescent medium for sound propagating through an inhomogeneous, moving fluid," J. Acoust. Soc. Am. **112**, 1269–1275 (2002).

[36]B. S. Melton and L. F. Bailey, "Multiple signal correlators," Geophysics **22**(3), 565–588 (1957).

[37]G. Averbuch, J. D. Assink, P. S. M. Smets, and L. G. Evers, "Extracting low signal-to-noise ratio events with the Hough transform from sparse array data," Geophysics **83**, WC43–WC51 (2018).

[38]P. S. M. Smets, L. G. Evers, S. P. Näsholm, and S. J. Gibbons, "Probabilistic infrasound propagation using," Geophys. Res. Lett. **42**, 6510–6517, https://doi.org/10.1002/2015GL064992 (2015).

[39]R. Buizza, M. Miller, and T. N. Palmer, "Stochastic representation of model uncertainties in the ECMWF Ensemble Prediction System," Q. J. Roy. Meteor. Soc. **125**(560), 2887–2908 (1999).

[40]R. Buizza, M. Leutbecher, and L. Isaksen, "Potential use of an ensemble of analyses in the ECMWF Ensemble Prediction System," Q. J. Roy. Meteor. Soc. **134**, 2051–2066 (2008).

[41]W. H. Munk, "Sound channel in an exponentially stratified ocean, with application to SOFAR," J. Acoust. Soc. Am. **55**, 220–226 (1974).

J. Acoust. Soc. Am. **147** (2), February 2020

Averbuch *et al.*   1077